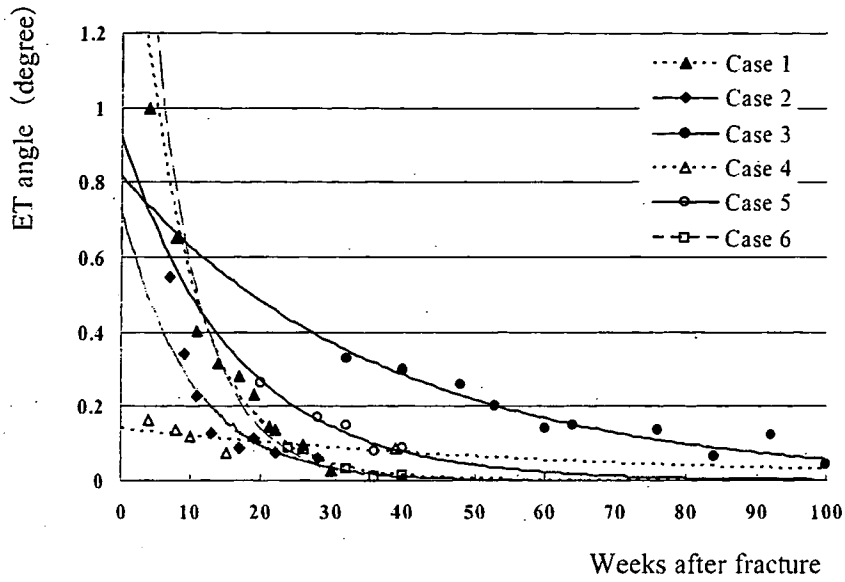

Fig. 8. In cases 1 through 6, the changes of the ET angle showed an exponential pattern. The correlation coefficients obtained by the regression equation for the ET angle and time were very high in these cases.

with considerable accuracy, sensitivity and reproducibility.

In patients with radiographically normal healing, the bending angle decreased exponentially over time. However, in patients with nonunion, the angle remained the same over time. According to the results obtained with previous methods such as the strain gauge method and the invasive method of Jernberger (1970), strain or deformation caused by loading at the healing site has been reported to diminish exponentially over time in patients with normal healing. Among these previous studies, Bourgois and Burny (1972) evaluated fracture healing in hundreds of patients treated with an external fixator that was instrumented with a strain gauge. They not only accumulated considerable clinical data on the strain readings over time, but also theoretically proved by mathematical simulation that the change of the strain over time during normal healing could be expressed as a typical hyperbolic curve. In addition to this, they proved that the time course of the change in strain could also be a hyperbolic curve by developing fracture simulation models with stabilization by intramedullary nailing, plating and external fixation. As a result, their clinical data were compatible with those for the theoretical model of external fixation. They classified the pattern of fracture healing into seven categories depending on the difference in the healing process. Among them, normal healing was defined as healing in which the strain reading *vs.* time curve reaches a plateau at 60 to 90 d after fracture. Slow healing was defined as healing in which the decline of strain was very slow compared with the normal pattern but the healing process was progressive over time. Nonunion was defined as cessation of the progress of healing. In two patients treated with a cast in our study, the ET angle decreased rapidly until 10 weeks after fracture to a level twice that on the intact side, and then it decreased slowly. The exponential regression curve for the echo tracking angle *vs.* time showed a very strong correlation (case 1, $r = -0.975$). Therefore, it can be concluded that the echo tracking method could be used to evaluate normal healing as proposed by Burny et al. (1984). As shown in Fig. 5, the progress of healing in patients treated with intramedullary nailing and bone grafting could be assessed by using the ET method. The ET angle *vs.* time relation in these cases was also expressed by exponential curves. However, the ET angle curve of patient 7 (Fig. 6b) did not show any significant decrease of the angle and there was no correlation between the ET angle and time. From this, the healing process was diagnosed as nonunion. The ET angle of patient 8, treated with plating, showed an extremely slow decrease over time from 9 weeks to 33 weeks, but reduction of the angle was statistically significant until 45 weeks, so the healing process was concluded to be delayed.

Fracture site stiffness was adopted as a parameter for evaluation that was thought to be correlated with strength of bone healing. In various earlier studies of fracture site mechanical properties, stiffness was measured to estimate the strength of the fracture site. However, stiffness is not necessarily correlated with strength. Chehade et al. (1997) investigated this relationship in 24

sheep. The tibia was stabilized with an external fixator and then osteotomy was done. Next, the tibiae were excised at 6, 8 and 10 wk after osteotomy and a 4-point bending test was done. As a result, in the initial stage of healing, stiffness showed a strong correlation with strength ($r = 0.89$), but there was no correlation between them in the remodeling stage. However, as Chehade et al. (1997) stated, because the stiffness of the fracture site is strongly correlated with the strength until remodeling is initiated, it is clinically significant to monitor fracture site stiffness as a substitute for strength to determine the appropriate level of weight bearing so that patients can avoid refracture because of overloading the fracture site during postoperative management. In the remodeling stage, we need to pay special attention to the relationship between stiffness and strength, even if stiffness reached the same value as the intact side.

Fracture healing was evaluated quantitatively by the echo tracking method in patients treated conservatively as well as by internal fixation. All previous methods of assessment could only be applied to patients treated with an external fixator that required the insertion of wires or screw pins, and none of the methods could achieve evaluation in a totally noninvasive manner. The potential problem with evaluating patients treated with internal osteosynthetic devices such as intramedullary nails or plates is that the stiffness at the fracture site is the sum of stiffness for both the healing fracture and the implant. The stiffness of the implant is very high compared with that of the healing fracture because it is made of a metal such as stainless steel or titanium-aluminum-vanadium alloy. Therefore, the combined stiffness at the fracture site is usually very high compared with that in patients receiving conservative treatment by casting. In such patients with internal osteosynthetic devices, comparison of stiffness with the intact side does not have any meaning for evaluation of fracture healing. Therefore, we have to be careful with interpretation of the changes of stiffness over time in such cases. How the implanted material and the configuration of stabilization affect fracture site stiffness should be investigated in the future so that we can assess fracture healing more precisely in patients with internal fixation.

In conclusion, it was demonstrated that the echo tracking method could be clinically applicable to evaluate fracture healing as a versatile, quantitative and noninvasive technique. Further development of this method should be performed so that it can be applied to other anatomical sites by improving accuracy and precision.

Acknowledgements—This work was funded in part by a grant from the Pharmaceutical and Medical Devices Agency of Japan.

REFERENCES

Bourgois R, Burny F. Measurement of the stiffness of fracture callus in vivo. A theoretical study. J Biomech 1972;5:85–91.

Burny F, Donkerwolcke M, Bourgois R, Domb M, Saric O. Twenty years experience in fracture healing measurement with strain gauges. Orthopedics 1984;7(12):1823–1826.

Chehade MJ, Pohl AP, Pearcy MJ, Nawana N. Clinical implications of stiffness and strength changes in fracture healing. J Bone Joint Surg [Br] 1997;79-B:9–12.

Hokanson DE, Mozersky DJ, Sumner DS, Strandness DEJ. A phase-locked echo tracking system for recording arterial diameter changes in vivo. J Appl Physiol 1972;32(5):728–733.

Jernberger A. Measurement of stability of tibial fractures. A mechanical method. Acta Orthop Scand 1970;135(suppl):1–88.

Matsuyama J, Ohnishi I, Sakai R, Suzuki H, Harada A, Bessho M, Matsumoto T, Nakamura K. A new method for measurement of bone deformation by echo tracking. Med Eng Phys 2006:28(6): 588–595.

Moorcroft CI, Ogrodnik PJ, Thomas PBM, Wade RH. Mechanical properties of callus in human tibial fractures: A preliminary investigation. Clin Biomech 2001;16:776–782.

Nicholls PJ, Berg E. Acoustic emission properties of callus. Med Biol Eng Comput 1981;19(4):416–418.

Watanabe Y, Minami G, Takeshita H, Fujii T, Takai S, Hirasawa Y. Prediction of mechanical properties of healing fractures using acoustic emission. J Orthop Res 2001;19(4):548–553.

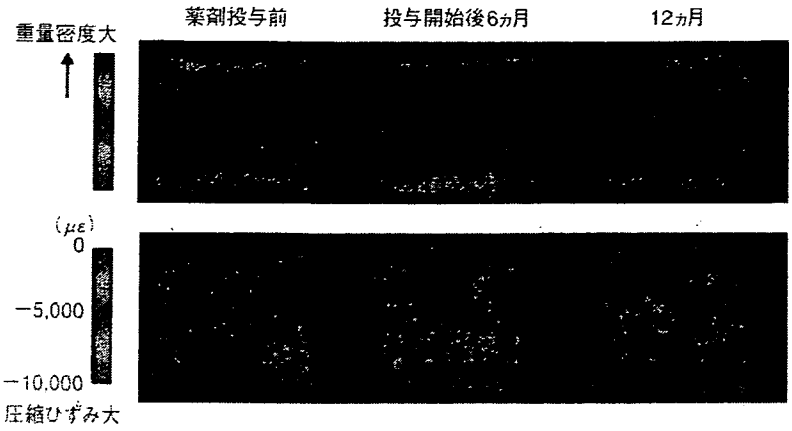

図2　74歳女性，アレンドロネート単独投与に伴う第2腰椎の重量密度および最小主ひずみ分布の変化

度解析値の解離がみられていた。

CT/有限要素法は骨強度だけではなく，骨力学特性を評価することが可能である。アレンドロネート投与開始6ヵ月でDXAによる骨密度が−0.9%低下に対しCT/有限要素法による椎体強度が33.3%増加，12ヵ月で骨密度が−0.3%低下に対し椎体強度が59.3%増加と，骨密度と椎体強度が解離した症例では，皮質シェルと隣接する海綿骨内の重量密度増加がみられ，最小主ひずみ分布で薬剤投与前では圧縮ひずみが著しく骨折が生じやすい領域に薬剤投与後では圧縮ひずみの減少がみられていた(**図2**)。

薬剤効果として，皮質シェル近傍の重量密度が増加するような骨基質分布の変化が起こり，圧縮応力の集中が軽減して最小主ひずみ分布が改善し，椎体強度が増加したと考えられ，DXAによる骨密度でとらえられない薬剤効果をCT/有限要素法で評価できる可能性が示唆された。

CT/有限要素法は骨密度に加え，ジオメトリー(geometry)，骨基質分布を含めて評価することが可能である。一方，CTの空間分解能に依存して骨微細構造や皮質骨の詳細な評価，マイクロダメージ(microdamage)の評価には限界があり，また骨代謝を評価することができない。さらに，DXAやpQCTに比較して放射線被曝量が多い点が検討すべき課題である。

おわりに

骨粗鬆症患者に対するアレンドロネート投与で，CT/有限要素法による椎体強度は，DXAによる骨密度より早期の投与開始後3ヵ月で薬剤効果を反映していた。薬剤効果として，骨密度増加だけではなく，骨基質分布の改善，骨折が生じやすい領域の最小主ひずみ分布の改善がみられていた。CT/有限要素法は，骨強度・骨力学特性の評価が可能という点で，骨粗鬆症治療薬の効果判定に有用と考えられる。

文　献

1) Imai K, Ohnishi I, Bessho M, Nakamura K. Nonlinear finite element model predicts vertebral bone strength and fracture site. Spine 2006;31:1789–94.
2) Keyak JH, Rossi SA, Jones KA, Skinner HB. Prediction of femoral fracture load using automated finite element modeling. J Biomech 1998;31:125–33.
3) Tucci JR, Tonino RP, Emkey RD, Peverly CA, Kher U, Santora AC, 2nd. Effect of three years of oral alendronate treatment in postmenopausal women with osteoporosis. Am J Med 1996;101:488–501.
4) Devogelaer JP, Broll H, Correa-Rotter R, Cumming DC, De Deuxchaisnes CN, Geusens P, et al. Oral alendronate induces progressive increases in bone mass of the spine, hip, and total body over 3 years in postmenopausal women with osteoporosis. Bone 1996;18:141–50.

5) Black DM, Cummings SR, Karpf DB, Cauley JA, Thompson DE, Nevitt MC, et al:Fracture Intervention Trial Research Group. Randomised trial of effect of alendronate on risk of fracture in women with existing vertebral fractures. Lancet 1996;348:1535-41.
6) Liberman UA, Weiss SR, Broll J, Minne HW, Quan H, Bell NH, et al: The Alendronate Phase III Osteoporosis Treatment Study Group. Effect of oral alendronate on bone mineral density and the incidence of fractures in postmenopausal osteoporosis. N Engl J Med 1995;333:1437-43.
7) Cummings SR, Black DM, Thompson DE, Applegate WB, Barrett-Connor E, Musliner TA, et al. Effect of alendronate on risk of fracture in women with low bone density but without vertebral fractures: results from the Fracture Intervention Trial. JAMA 1998;280:2077-82.
8) Pols HA, Felsenberg D, Hanley DA, Stepan J, Munoz-Torres M, Wilkin TJ, et al: Fosamax International Trial Study Group. Multinational, placebo-controlled, randomized trial of the effects of alendronate on bone density and fracture risk in postmenopausal women with low bone mass: results of the FOSIT study. Osteoporos Int 1999;9:461-8.
9) Ensrud KE, Black DM, Palermo L, Bauer DC, Barrett-Connor E, Quandt SA, et al. Treatment with alendronate prevents fractures in women at highest risk: results from the Fracture Intervention Trial. Arch Intern Med 1997;157:2617-24.

07(IV)-19

直達式骨折整復の臨床データ取得システム

○ 鄭 常賢[a], 廖洪恩[b], 小林英津子[b], 光石衛[b], 中島義和[b], 小山毅[d], 菅野伸彦[d], 前田ゆき[e], 別所雅彦[c], 大橋暁[c], 松本卓也[c], 大西五三男[c], 佐久間一郎[b]

東京大学大学院{[a]新領域創成科学研究科, [b]工学系研究科, [c]医学系研究科}, [d]大阪大学大学院医学系研究科, [e]大阪南医療センター

A Clinical Data logging system of Direct fracture reduction.

S.Joung[a], H.Liao[b], E.Kobayashi[b], M.Mitsuishi[b], Y.Nakajima[b], T.Koyama[d], N.Sugano[d], Y.Maeda[e], M.Bessho[c], A.Ohashi[c], T.Matsumoto[c], I.Ohnishi[c], I.Sakuma[b]

{[a]Graduate School of Frontier Sciences, [b]Graduate School of Engineering, [c]Graduate School of Medicine}, the University of Tokyo,

[d]Graduate School of Medicine, Osaka University, [e]National Organization Osaka Minami Medical Center

Abstract: Clinical data quantification of a fracture reduction has become important as the development of new fracture reduction technology such as navigation and robot assisted fracture reduction. A reduction force and a reduction path are the key points in considering the control and safety of these new reduction methods. We have developed a clinical data logging system(CDLS) of direct fracture reduction, which reduces using ring-frame connected bone fragment directly. The CDLS synchronously records the reduction force, the reduction path and two video signals. One records the images from C-arm and the other records whole surgery process. This paper introduces the structure of CLDS and the resultants of application to fracture model.

Key words: Clinical data, Fracture reduction, Reduction force, Reduction path.

1. 序論

骨折治療は近年大きく発展してきており, 低侵襲で整復の精度を上げることが可能となってきた. 特に最近は, 術中に骨片の位置が認知できるナビゲーションシステムを用いた治療方法に関する研究が盛んに行われている [1]. 骨折治療法は様々であるが, どの治療法でも整復を伴い整復の結果が治療の成果に大きく影響する. 大腿骨頚部骨折の整復に関しては大きい整復力が必要で術者への負担が過大になる. そこで, ロボットを用いた整復支援システムに関する研究が報告されている [2, 3]. このような整復支援ロボットには過渡の整復力を防ぐための安全装置が装着されている. 一定以上の整復力が働いたときにその軸がフリー状態になるフェイルセイフ装置が一例である[3].

ロボットの制御方法と安全装置の仕様を決めるためには, 整復手術中の整復パス, 整復力などの臨床データを参照するべきであり, 今までは大きく必要とされていなかった骨折整復術中の臨床データを記録し定量化する必要性が整復技術の発展と共に高くなってきた. このため, Thomas らは整復力を定量化した[4]. しかし, 整復パスを記録していないため骨片の位置と整復力との関係は解析されていない. そこで我々は骨片に打ったピンをリングフレームで固定し, そのフレームを持ち骨折整復を行う直達式整復術中の整復力とパスを記録するシステムを開発した[5]. しかし, 整復力を計測するセンサの滅菌を検討してなかったので, 臨床使用には適してなかった. 本研究では, 臨床使用可能とするように改良し, さらに画像入力も可能としたシステムを紹介し, 模擬骨を用いた整復への応用結果を報告する.

2. 臨床データ取得システム

臨床データ取得システム(Clinical Data loggings system, CDLS)では骨折整復時に発生する整復力, 整復パス, C-arm画像と現場の様子を記録することが望ましい. 我々の開発した CDLS は, PC,画像入力ボード (PCI-5531, Interface), 整復力を測るための力覚センサ (IFS-67M25T50, Nitta, 定格 Fx, Fy [N]: 450; Fz [N]: 900; Mx - Mz [Nm]:40), 整復パスを追跡するための光学式 3 次元位置計測装置(Polaris, NDI, Canada)で構成され, 以上のデータを計測可能とした. これらのデータは位置と整復力との関係などを分析するため, 同期を取って記録する必要があり, システムではひとつのプロセスでコンピュータ側からデータ要求信号を送りそのときのデータを取得する方法を用いた.

Thomas らの研究結果によると骨片の牽引力の最大値は396N, 回旋トルクの最大値は74Nmなので使用した力覚センサの定格は十分である. しかし, 力センサの適切な滅菌法がないため, 滅菌可能なカバーを製作した. カバーはアシスタントの補助により, 術者の手を汚すことなく, 取り付けられる. Fig. 1にカバーを取り付けた力覚センサと整復装置の外観を示す. 図の右はカバーを外したときのセンサとカバーの様子である. カバーには整復パスを記録するため, 光学式 3 次元位置計測装置のマーカを付着した. 骨片の位置と整復力を計算するための概念図を

Fig. 2 に示す. 光学式 3 次元位置計測装置, 力覚センサ, C-armと骨片の座標系を各々ΣP, ΣS, ΣC, ΣBと設定する. ΣPからΣSとΣC への変換行列 ${}^{P}T_{S}$ と ${}^{P}T_{C}$ は 3 次元計測器から計測できる. ΣC からΣBへの変換行列 ${}^{C}T_{B}$ は 2D/3D レジストレーションなどの手法で求められる. 以上の変換行列で力覚センサの座標系から骨座標系への変換行列 ${}^{S}T_{B}$ が式(1)で計算できる.

$$ {}^{S}T_{B} = \left({}^{P}T_{S}\right)^{-1} {}^{P}T_{C}\, {}^{C}T_{B} \tag{1} $$

そこで骨片と整復装置を剛体として考えると, ${}^{S}T_{B}$ を一回計算しておくことにより, 整復中はセンサのマーカを追跡することたけで光学式 3 次元位置測装置から見た骨の位置と姿勢が式(2)で求められる.

$$ {}^{P}T_{B} = {}^{P}T_{S}\, {}^{S}T_{B} \tag{2} $$

整復力に関しても, 式(3)(4)により, センサから計測した力が骨座標系の力に変換できる.

$$ {}^{B}T_{S} = ({}^{S}T_{B})^{-1} = \begin{bmatrix} {}^{B}R_{S} & {}^{B}P_{S} \\ 0 & 1 \end{bmatrix} \tag{3} $$

$$ \begin{bmatrix} {}^{bone}\mathbf{f} \\ {}^{bone}\mathbf{n} \end{bmatrix} = \begin{bmatrix} {}^{B}R_{S} & \mathbf{0} \\ \left[{}^{B}P_{S}\times\right]{}^{B}R_{S} & {}^{B}R_{S} \end{bmatrix} \begin{bmatrix} {}^{sensor}\mathbf{f} \\ {}^{sensor}\mathbf{n} \end{bmatrix} \tag{4} $$

3. 骨折モデルの整復への応用

骨折モデルは X 線で確認できる材質のモデル骨を骨折させ, 筋肉代わりにゴムを貼り付けることで製作した. 大腿骨頚部骨折の場合, 骨片は中殿筋, 外閉鎖筋などの働きにより上半身のほうに引っ張られ, 外旋されるのでその働きをゴムで模擬した. 今回の実験では骨の座標はペンマーカを用いて指定した. 整復は整形外科医により行い, そのときのデータを CDLS により取得した. C-armは使わず, 代わりにカメラからの画像を入力した.

データの取得周期 0.3s で 2 枚の画像, 整復力と整復パスを記録することができた. Fig. 3 に取得した整復力を示す. 整復力はy軸の力(牽引方向)とモーメント(内旋方向)に大きく必要とすることが解る. 整復パスはマーカが術者に隠され一部記録できてない部分があった.

4. 考察と結論

実験では模擬骨を用いたので, 計測した整復力の大きさには意味がないが, どの成分の整復力が働くか確認することができた. また整復時の骨片の動きも確認することができた. センサのマーカは術者に邪魔にならない横方向に移すべきである. データ取得周期は 0.3 秒で遅いが, 整復の動作がゆっくり行われるので問題にはならない. 周期をあげるためには複数のパソコンにより並列処理をすればよいが, システムが大きくなるので手術現場では適さない.

今後は, C-armとレジストレーション方法を用いた模擬整復でシステムを評価し, 実際に臨床でデータ取得を行う予定である.

謝辞

本研究の一部は厚生労働科学研究費補助金(生体機能解析・補助・代替機器開発研究事業)(17100301)による.

文献

1) P.Grützner, et al.:"Computer aided long bone fracture treatment", Injry, Int.J.Care injured(2004) 35, S-A57-S-A64, 2004
2) B. Füchtmeier, et al.:"Reduction of femoral shaft fractures in vitro by a new developed reduction robot system 'RepoRobo'", Injury, Int.J.Care Injured (2004)35, S-A113-S-A119, 2004
3) Mamoru MITSUISHI, et al.: "Development of a Computer-Integrated Femoral Head Fracture Reduction System", Proceedings of the 2005 IEEE International Conference on Mechatronics,834-839, 2005
4) Thomas Gösing, et al.: "Force and Torque during Fracture Reduction: Intraoperative Measurements in the Femur", Journal of Orthopaedic Research, 333-338,2006
5) 森本顕二郎 他, " 直達式骨折整復支援装置に関する研究" 第15回日本コンピュータ外科学会大会論文集, 2006

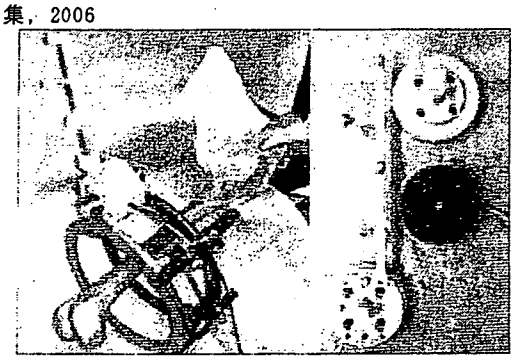

Fig. 1 Fracture reduction device.

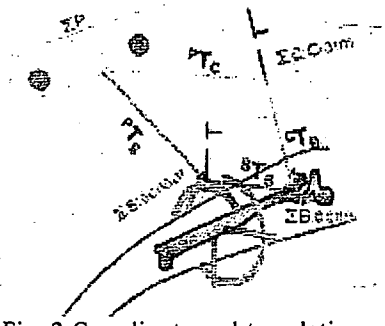

Fig. 2 Coordinate and translation matrix.

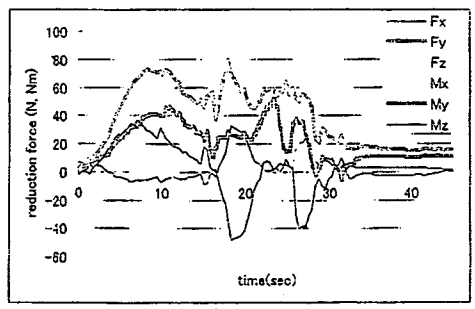

Fig.3 The reduction force during fracture reduction

直達式骨折整復を支援する骨折整復システムの開発

鄭 常賢[1]、加門 大和[1]、廖 洪恩[2]、光石 衛[2]、中島 義和[2]、
小山 毅[4]、菅野 伸彦[4]、前田 ゆき[5]、別所 雅彦[3]、大橋 暁[3]、松本 卓也[3]、
岩城 純一郎[6]、中沢 東治[6]、大西 五三男[3]、中村 耕三[3]、佐久間 一郎[2]
東京大学大学院｛[1]新領域創成科学研究科、[2]工学系研究科、[3]医学系研究科｝
[4]大阪大学大学院 医学系研究科、[5]大阪南医療センター、[6]THK(株)

骨粗鬆症がある患者におこりやすい骨折のなかでも大腿骨頚部骨折は寝たきりとなる可能性の高い骨折である。社会の高齢化の進行に伴い骨粗鬆症の患者が増加すると、大腿骨頚部骨折の患者も増加すると予測されている。

大腿骨頚部骨折の治療法は外科的な手術によるものがほとんどである。手術では大腿骨の遠位骨片を牽引しながら位置決めし、ピンによって固定する。しかし、大腿筋などの周辺組織が萎縮した状態では整復のための牽引に大きな力が必要となるため術者にとって負担となる。また、X線透視下で2次元の情報を用いて位置決めを行わなければならないため、術者の熟練が必要であり、手術を行うことで術者が受けるX線被爆も問題である。

これらの問題に対し、我々は骨折整復システムの開発を行った(Fig. 1)。システムは骨折整復ロボットとナビゲーションシステムに構成されている。骨折整復には、足首をつかみ遠位骨片の位置を合わせる介達式骨折整復方法と、骨片にピンを打ち、ピンに連結されたリングを持って直接整復を行う直達式骨折整復方法がある。骨折整復システムは介達式骨折整復に対して使えるように構成されているが、ロボットを使う利点を考えると骨片の正確な位置決めが可能な直達式骨折整復にも使用されるように構成する必要があり、今回は新たに直達式骨折整復を直達式骨折整復ロボットに実装を行った。

骨折整復ロボットは並進3自由度と回転3自由度の6自由度を有する。骨片の牽引と回旋をするときの整復力が設定値より大きくなると各関連軸をフリーにするフェイルセイフ装置が装着されており安全性を保つ。動作モードはタッチパネルを用いたジョグモード、術者の整復力をパワーアシストする手動モード、ナビゲーションからの指令により自動で整復を行う自動整復モードがある。

直達式整復では、骨とロボットの手先は専用のジグで繋がっているので、骨の長軸とロボットの牽引軸が一致しない。骨片の姿勢だけを変えるため、骨折断面の中心を仮想中心と見なし、ロボットを制御する拘束パワーアシストを実装し、有効性を検証した。

ナビゲーションシステムは術前にCTからの3次元モデルを用いて整復ゴールを計算する。術中にはC-armで撮った画像と3次元モデルをレジストレーションすることにより、実空間での骨片間の位置関係を認知する。骨片の現在位置からゴールまでの整復パスは術者の意見を反映して作成され、整復ロボットに指令を送り整復を行う。構成したシステムは骨折モデルでの整復実験でその有効性を示す。

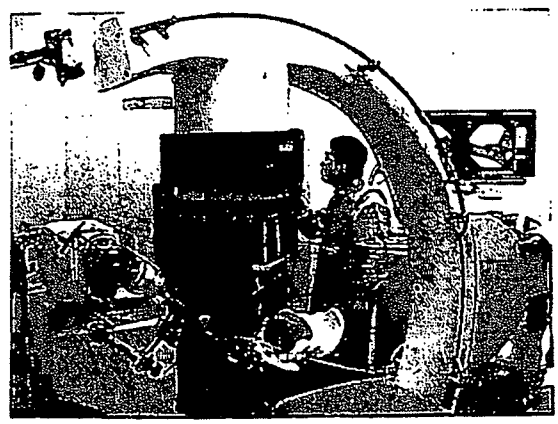

Fig.1. 骨折整復システム

A Parallel Implementation of 2-D/3-D Image Registration for Computer-Assisted Surgery

Fumihiko Ino[1], Yasuhiro Kawasaki[1], Takahito Tashiro[1], Yoshikazu Nakajima[2], Yoshinobu Sato[2], Shinichi Tamura[2], and Kenichi Hagihara[1]

[1]Graduate School of Information Science and Technology, Osaka University
[2]Graduate School of Medicine, Osaka University

Abstract

This paper presents the design and implementation of a parallel two-dimensional/three-dimensional (2-D/3-D) image registration method for computer-assisted surgery. Our method exploits data and speculative parallelism, aiming at making computation time short enough to carry out registration tasks during surgery. Our experiments show that exploiting both parallelisms reduces computation time on a cluster of 64 PCs from a few tens of minutes to less than a few tens of seconds.

1. Introduction

Image registration is a technique for finding point correspondences between two different images taken usually at different times, from different viewing points, and/or in different modalities. This technique plays an increasingly important role in surgery. For example, registration of preoperative images to intraoperative images is essential to perform image-guided and robot-assisted surgery [6], which minimizes surgical complications for better surgical outcomes.

For this purpose, many researchers have tackled the problem of 2-D/3-D registration [1], which estimates the location and orientation of a 3-D volume with respect to the patient coordinate system using one or more 2-D projected images. The reason why aligning a 3-D volume to 2-D images is due to the limitations of current 3-D imaging systems, such as computed tomography (CT) scans, which have more spatial information but require more acquisition time and radiation exposure, as compared with 2-D imaging systems. Due to these limitations, the intraoperative data is usually 2-D X-ray fluoroscopy or ultrasound images, whereas the preoperative data is 3-D CT volumes, motivating us to deal with 2-D/3-D registration.

One key challenge for 2-D/3-D registration is to develop a fast, accurate, and robust algorithm. Prior algorithms can be classified into two groups: feature- and intensity-based approaches. The intensity-based approach [1,5,6] has been shown to provide more accurate and robust results than the feature-based approach [3,7]. The intensity-based approach compares the intensity values between the real projected image and the digitally reconstructed radiograph (DRR) generated from the volume. It requires a large amount of computation to iteratively produce DRRs until a best match between the projected image and the DRR is found. Therefore, acceleration strategies are required to minimize surgical time.

In this paper, we present the design and implementation of a parallel 2-D/3-D registration method, aiming at achieving fast, accurate, and robust alignments for computer-assisted surgery. Our method parallelizes an intensity-based algorithm to reduce computation time without degrading the quality of alignment. The key contribution of our method is to provide fast and robust alignments by means of data-parallel and speculative processing, respectively.

2. Intensity-Based 2-D/3-D Registration

The intensity-based algorithm employed in our method has the following three advantages: (1) automated registration by comparing a real projected image and a DRR [1]; (2) robust registration using an information-based similarity measure [5]; and (3) accurate registration using biplane 2-D images [2] and region of interest (ROI) [6]. Due to the limited space, we describe only advantages (1) and (2).

Before describing each advantage, we first define the 2-D/3-D registration problem. To make it easier, we present a definition for a single image rather than biplane images. Given a volume V and a real projected image I_F (see Figure 1), the 2-D/3-D registration technique computes the rigid transformation parameter $\mathbf{T}$ that relates the coordinate system of the volume V and that of the imaging (patient) environment. Here, the rigid transformation is given by $\mathbf{T} = (T_X, T_Y, T_Z, \theta_X, \theta_Y, \theta_Z)$, where the first and last three parameters are the translations and rotations of V.

Figure 2 briefly presents the intensity-based algorithm. The algorithm resolves the registration problem into an optimization problem. That is, in order to register the volume V to the 2-D image I_F, the algorithm optimizes a cost function C associated with the location and orientation of V,

Proceedings of the 2005 11th International Conference on Parallel and Distributed Systems (ICPADS'05)
0-7695-2281-5/05 $20.00 © 2005 IEEE

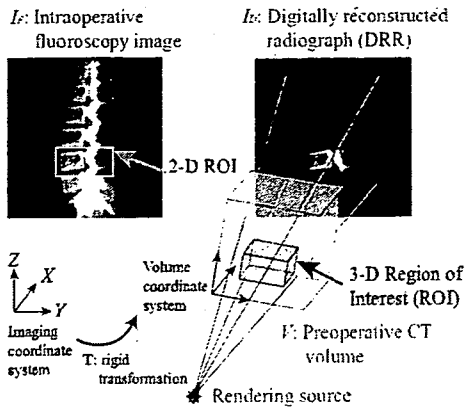

Figure 1. Overview of intensity-based 2-D/3-D registration. In this case, it aligns a CT volume of a real spine to a fluoroscopy image of the spine.

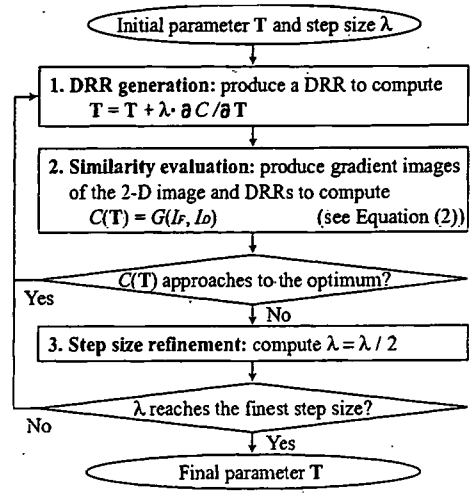

Figure 2. Intensity-based 2-D/3-D registration algorithm.

where C represents the similarity measure between the 2-D image I_F and the DRR I_D, generated from V. Furthermore, this optimization is performed in a hierarchical manner in order to reduce the amount of computation. This hierarchy is controlled by the step size λ of the optimization.

The algorithm consists of the following technologies.

DRR generation: As illustrated in Figure 1, a ray casting method generates the DRR I_D. Image intensity $I_D(i,j)$ at point (i,j) on the DRR I_D is computed by accumulating the intensities of the voxels that ray $\mathbf{r}(i,j)$ penetrates, where $\mathbf{r}(i,j)$ represents a ray that penetrates point (i,j) from the rendering source.

Similarity measure: We use gradient correlation (GC) for our algorithm according to an experimental study [5] on six similarity measures. Although the study found that pattern intensity [6] and gradient difference were the most robust measure for their registration scenario, these measures require intensity correction [5] to minimize the difference between the two images I_F and I_D, because they use a difference image created by subtracting I_D from I_F. In contrast, GC focuses on edge information in the images, so it essentially does not require intensity correction to minimize the difference. Furthermore, the study also showed that GC provided a small failure rate (5%) for clinical datasets, and it was the most robust measure that assumed no intensity correction. Therefore, we use GC as the similarity measure between the two images I_F and I_D: $C(\mathbf{T}) = G(I_F, I_D)$. Here, GC $G(A,B)$ between images A and B is given by $G(A,B) = N/2\,(\partial A/\partial i, \partial B/\partial i) + N/2\,(\partial A/\partial j, \partial B/\partial j)$, where $\partial A/\partial i$ and $\partial A/\partial j$ ($\partial B/\partial i$ and $\partial B/\partial j$) are the gradient images of A (B, respectively), representing the derivative of the intensity in the horizontal and vertical axes of the image, and $N(A,B)$ is normalized cross correlation (NCC) defined over two images A and B.

The gradient images are produced by means of the first derivative of a Gaussian. This filter has the advantage that it reduces and smoothes noise in the images, improving the robustness of alignment. In summary, the intensity values at point (i,j) on the gradient images $\partial A/\partial i$ and $\partial A/\partial j$ are given by convolution with the first derivative Gaussian filters $F_I(i,j)$ and $F_J(i,j)$: $\partial A(i,j)/\partial i = F_I(i,j) * A(i,j)$ and $\partial A(i,j)/\partial j = F_J(i,j) * A(i,j)$, where $F_I(i,j) = \frac{-i}{2\pi\sigma^4} e^{-(i^2+j^2)/2\sigma^2}$, $F_J(i,j) = \frac{-j}{2\pi\sigma^4} e^{-(i^2+j^2)/2\sigma^2}$, and σ is the standard deviation of the distribution and is proportional to the kernel size, namely the size of neighborhood on which the filter operates.

Summarizing the above description, the main computation phases of the algorithm are (a) DRR generation, (b) gradient image generation, and (c) NCC computation.

Optimization: In order to find the optimal transformation parameter $\mathbf{T}$ that maximizes the cost function C, the algorithm employs the steepest descent optimization technique during registration process: $\mathbf{T} = \mathbf{T} + \lambda \partial C/\partial \mathbf{T}$. This optimization stops if a local optimum has been found. The gradient $\partial C/\partial \mathbf{T}$ of the cost function is estimated by using the finite-difference approximation. Because the transformation $\mathbf{T}$ consists of six independent parameters, the computation phases (a)–(c) are repeated 13 times to approximate the gradient $\partial C/\partial \mathbf{T}$ at each optimization step: one repetition for current transformation $\mathbf{T}$ and 12 repetitions for finite differences $\mathbf{T} \pm \lambda\Delta$ of each parameter.

3. Parallelizing 2-D/3-D Registration

In this section we present the design and implementation of our parallel method.

Proceedings of the 2005 11th International Conference on Parallel and Distributed Systems (ICPADS'05)
0-7695-2281-5/05 $20.00 © 2005 IEEE

3.1. Design Aspects

To accelerate the registration process, we can exploit three parallelisms as follows.

- Speculative parallelism: In the registration algorithm, speculative parallelism can be exploited by simultaneously processing the same registration task with different initial parameters. This is important to prevent unsuccessful registrations (due to local optimums), because the surgery cannot progress until the alignment has correctly finished. Otherwise, the surgery must be performed without the surgical plan. To prevent such undesirable situations, an appropriate transformation is required as the initial parameter T. However, in general, initial parameters are experimentally determined according to the surgeon's experience. Therefore, speculative processing contributes to improve the robustness and confidence of our method.
- Data parallelism: Exploiting this parallelism accelerates a single registration task. It can easily be established by using image parallelism [4], where processors take the responsibility for each subtask associated with a small part of the 2-D image. The details are presented later in Section 3.2.
- Task parallelism: This parallelism also contributes to accelerate a single registration task. It exists in the finite-difference approximation, where the computation phases (a)–(c) are repeated 13 times. However, this means that the speedup derived by this parallelism is limited by a small factor of 13. Furthermore, load balancing is probably not easy if it is exploited, because 13 cannot divide the number of processors, usually chosen to be a power of two.

From the above discussion, we have decided to exploit speculative and data parallelism.

In addition to the computation phases (a)–(c), input/output (I/O) operations also might become a performance bottleneck after parallelization. However, I/O issues are not critical in our cluster environment for the following two reasons. Firstly, the largest input data, namely the volume V, is the preoperative data, which can be distributed to processors before surgery. Therefore, we can assume that processors have loaded it into their local memory when registration tasks are submitted. Secondly, the remaining data I_F is small enough to be broadcasted rapidly in our cluster. Therefore, we assume that all processors have the entire data, V and I_F, in their local memory.

3.2. Workload Distribution

We now present how our method exploits image parallelism. A good solution to this issue balances workload among processors and minimizes the amount of messages transmitted between processors and the number of sends and receives. To find such a solution, we first investigate the characteristics of computation phases (a)–(c) with respect to available parallelism, load balancing, and data access pattern. Table 1 shows these characteristics with a preliminary timing result measured on a single processor machine.

- DRR generation: The intensity value at any point (i, j) can independently be computed with the values at other points, because different rays can cast independently. The workload associated with each point is nonuniform due to the different number of penetrated voxels. Points around the DRR edge tend to have less workload. In addition to this image parallelism, we also can use object parallelism [4], where processors take the responsibility for each subtask associated with a small part of the volume and then merge locally rendered DRRs into a final DRR. This object-parallel scheme allows processors to load only a small portion of the volume, but it requires communication to generate the final DRR. As mentioned earlier, we assume that all processors have the entire volume, so that our method uses an image-parallel scheme to prevent communication in this most time-consuming phase.
- Gradient image generation: As same as in DRR generation, different points can independently be processed to obtain their intensities on the gradient image. The convolution for point (i, j) requires all intensities $A(i+\alpha, j+\beta)$ such that $-\lfloor K/2 \rfloor \leq \alpha, \beta \leq \lfloor K/2 \rfloor$, where K denotes the kernel size of the filter. Note here that this means any point on the gradient image requires DRR generation of its surrounding $K \times K$ neighborhood, because the gradient images are generated from the DRR I_D as well as the image I_F. With regard to load balancing, this computation phase has uniform workload, because the same kernel size K is used for every point. Note also here that the kernel size K is usually a relatively large number, which increases the amount of messages under an inappropriate workload distribution scheme. For example, we use $K = 19$ pixels for typical 2-D ROI sizes ranging from 200×200 to 400×400 pixels.
- NCC computation: NCC computation can be approached as a reduction problem, because it can be rewritten as $N(A,B) = \sum_{i,j} \left(A(i,j)B(i,j) - \overline{A}\,\overline{B}\right) / \sqrt{\sum_{i,j}(A(i,j)^2 - \overline{A}^2)}\sqrt{\sum_{i,j}(B(i,j)^2 - \overline{B}^2)}$. This equation indicates that NCC can be computed from six local sums: the local sums of the number of points; intensities $A(i,j)$; $B(i,j)$; squared intensities $A(i,j)^2$; $B(i,j)^2$; and multiplied intensities $A(i,j)B(i,j)$. These sums can independently be computed if processors are responsible for the same point (i, j) on images A and B. The workload is perfectly balanced if the same number of points is assigned to each processor. However, communication is required to reduce local sums into a global sum.

According to the analysis mentioned above, our method employs a 2-D block distribution scheme with the overlap

Proceedings of the 2005 11th International Conference on Parallel and Distributed Systems (ICPADS'05)
0-7695-2281-5/05 $20.00 © 2005 IEEE

Table 1. Summary of computation phases.

Computation phase	Parallelism	Workload	Data required for intensity $A(i,j)$	Time (s)
(a) DRR generation	Image/object[1]	Nonuniform	Penetrated voxels	993.7
(b) Gradient image generation	Image	Uniform	Surrounding $K \times K$ neighborhood intensities	67.2
(c) NCC computation	Image[2]	Uniform	Corresponding intensity $B(i,j)$	2.5

1, 2: Communication is required to produce the final DRR and to perform reduction operations, respectively.

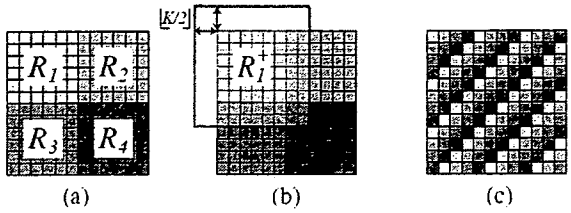

Figure 3. Workload distribution.

region, as shown in Figure 3. Here, the overlap size is given by the kernel size K, allowing processors to produce gradient images without any communication. As compared with other distribution schemes such as 1-D/2-D disjoint block and cyclic schemes, our scheme has the following advantage/disadvantages: (1) less communication, achieved by the overlap region; (2) more computation, due to the redundant DRR generation for the overlap region; and (3) imbalanced workload, as compared with the cyclic scheme.

If the overlap region is not given, communication is required for block boundaries in order to obtain intensities of neighbor points computed by other processors. This communication becomes a significant performance bottleneck in a case where many processors are responsible for the neighbor points. In this case, processors need to gather the intensities from many processors and also have to scatter their own intensities to others, but it is not easy to realize both fast scatter and gather operations at the same time. Due to this complex communication pattern, the cyclic scheme possibly results in poor performance. Furthermore, the 1-D/2-D block scheme without the overlap will also suffer from this situation as the number of processors P increases, because the kernel size K is relatively large compared to the block size, which decreases as P increases.

3.3. Proposed Method

We denote by $\mathcal{R} = \{(i,j) \mid 1 \le i \le S_I, 1 \le j \le S_J\}$ the domain of the ROI specified on the 2-D image, where S_I and S_J are the horizontal and vertical size of the ROI, respectively. Let $\mathcal{R}_p$, where $1 \le p \le P$, be the p-th subdomain partitioned by the 2-D disjoint block scheme such that $\mathcal{R} = \bigcup_{p=1}^{P} \mathcal{R}_p$ and $\mathcal{R}_p \bigcap \mathcal{R}_q = \emptyset$, for all $1 \le p < q \le P$. Let $\mathcal{R}_p^+$ be the p-th subdomain with its overlap region.

Given P processors, our parallel method aligns the volume V to the image I_F as follows.

1. Data load: For all $1 \le p \le P$, processor p loads the volume V from its local disk into main memory, and waits for registration tasks to be submitted. Then, processor 1 serves as a gateway receiving a registration task with its input data: the projected image I_F, the initial parameter $\mathbf{T}$, and the initial step size λ. After this, the gateway broadcasts the data to all processors.
2. DRR generation: For all $1 \le p \le P$, processor p locally generates a DRR for subdomain $\mathcal{R}_p^+$.
3. Gradient image generation: For all $1 \le p \le P$, processor p locally generates the gradient images for disjoint subdomain $\mathcal{R}_p$.
4. NCC computation: For all $1 \le p \le P$, processor p locally computes six local sums from subdomain $\mathcal{R}_p$. Then, every processor participates in a reduction communication to combine local sums from all processors and distribute the global sum back to all processors. After this communication, every processor has six global sums, so that locally computes NCC.
5. Optimization: Repeat 2.–4. 13 times to update the parameter $\mathbf{T}$ by using the steepest descent optimization. Repeat this step until a local optimum has been found.

4. Experimental Results

To evaluate the performance of our parallel method, we have implemented it using the C++ language and Message Passing Interface (MPI) standard.

We used a cluster of 64 PCs, each equipped with two Pentium III 1-GHz processors. The interconnection between nodes is a Myrinet switch, yielding a bandwidth of 2 Gb/s. Our implementation runs on a Linux operating system with the MPICH-SCore library, a fast MPI implementation.

On timing results. We performed registration tasks using datasets of a femur phantom and a real spine (see Table 2). The biplane images are generated as the front (coronal) view and the side (sagittal) view of the body. The kernel size K of the Gaussian filter was experimentally determined as $K = 19$ pixels ($\sigma = 3$).

We produced the CT volume and distributed it with its ROI information to each node before running our registration program. This distribution takes 1.7 and 3.8 s on the Myrinet network for the femur and the spine datasets, respectively. On the other hand, the 2-D fluoroscopy images are produced immediately before registration and then are broadcast by the registration program itself. It takes 37 and 119 ms to broadcast each dataset, respectively.

Proceedings of the 2005 11th International Conference on Parallel and Distributed Systems (ICPADS'05)
0-7695-2281-5/05 $20.00 © 2005 IEEE

Table 2. Dataset specification.

	Femur phantom	Real spine
3-D volume size	256 × 256 × 367	512 × 512 × 204
File size	45 MB	102 MB
ROI size	53 × 47 × 54	299 × 299 × 47
2-D image size	640 × 512	1024 × 1024
File size	320 KB	2 MB
ROI size (front)	353 × 276	340 × 204
ROI size (side)	344 × 272	336 × 200

Table 3. Registration time and speedups.

# of procs P	Femur phantom		Real spine	
	Time (s)	Speedup	Time (s)	Speedup
1	320	1	1066	1
8	52	6	171	6
16	31	10	101	11
32	19	17	62	17
64	13	26	44	24
128	9	35	35	31

Table 3 shows experimental timing results on different numbers of processors. We can see that our implementation running on $P = 128$ reduces computation time for the spine dataset from 17 m (1066 s) to 35 s. It also achieves a shorter time of 9 s for the femur dataset with a smaller ROI. Times of less than 60 s are compatible with time constraints required for surgery. Thus, our parallel method enables us to utilize registration technique during surgery without degrading the quality of alignment.

On workload distribution. If we change our distribution scheme to a 1-D block scheme with overlap, the size of disjoint blocks and that of overlapping blocks on $P = 128$ become 3×276 and 21×294 pixels, respectively. Therefore, this 1-D scheme requires about 7.5 times more computation, resulting in a lower speedup. Moreover, since the vertical length of 1-D blocks becomes shorter than that K of the filter, processors need to communicate with more processors to obtain intensities of vertical neighbors, having a more complex communication pattern with network contention.

Although our overlapping scheme requires redundant computation for DRR generation, this disadvantage is covered by the advantage of less communication. If a 2-D disjoint block scheme is employed, every processor needs to communicate its boundary data with its vertical/horizontal/diagonal neighbors. Though this can be implemented by repeating shift communication operations, these operations could be a performance bottleneck. For example, when using 128 processors for the femur dataset, this scheme causes 2.7 KB ($41 \cdot 53 - 23 \cdot 35$ pixels, each in 2 bytes) of incoming data and the same amount of outgoing data at every processor, which must be sequentially processed in eight shift communication operations.

On speculative processing. In our experiments, we found that the speedup was limited by a relatively smaller value, as compared with P. In this situation, where the speedup is theoretically limited by a small value, using more processors for data-parallel processing results in a lower utilization of computing nodes. To deal with this, our method tries to raise the speedup by means of speculative processing. This strategy will lead to a higher speedup if registration tasks are repeatedly processed with different initial parameters due to unsuccessful alignments.

Another important motivation to exploit speculative parallelism comes from the fact the registration algorithm sometimes fails to align objects due to local optimums. Therefore, our strategy will also improve the confidence of registration technique, providing more robust alignment for a wide variety of clinical scenarios.

5. Conclusions and Future Work

We have presented a parallel method for 2-D/3-D registration, aiming at realizing intraoperative alignment. Our method exploits data and speculative parallelism in an intensity-based algorithm, so that can perform fast, accurate, and robust registration during surgery. Our implementation on a cluster of 64 PCs aligns a $299 \times 299 \times 47$ voxel volume to 340×204 pixel images in a few tens of seconds, a clinically compatible time.

In the future, our parallel implementation could be improved by exploiting task parallelism in order to achieve further acceleration.

References

[1] L. Lemieux, R. Jagoe, D. R. Fish, N. D. Kitchen, and D. G. T. Thomas. A patient-to-computed-tomography image registration method based on digitally reconstructed radiographs. *Medical Physics*, 21(11):1749–1760, Nov. 1994.

[2] S. Li, C. A. Pelizzari, and G. T. Y. Chen. Unfolding patient motion with biplane radiographs. *Medical Physics*, 21(9):1369–1512, Sept. 1994.

[3] R. A. McLaughlin, J. Hipwell, D. J. Hawkes, J. A. Noble, J. V. Bryne, and T. Cox. A comparison of 2D-3D intensity-based registration and feature-based registration for neurointerventions. In *Proc. MICCAI'02, Part II*, pages 517–524, Sept. 2002.

[4] S. Molnar, M. Cox, D. Ellsworth, and H. Fuchs. A sorting classification of parallel rendering. *IEEE Computer Graphics and Applications*, 14(4):23–32, July 1994.

[5] G. P. Penny, J. Weese, J. A. Little, P. Desmedt, D. L. G. Hill, and D. J. Hawkes. A comparison of similarity measures for use in 2-D–3-D medical image registration. *IEEE Trans. Medical Imaging*, 17(4):586–595, Aug. 1998.

[6] J. Weese, G. P. Penney, P. Desmedt, T. M. Buzug, D. L. G. Hill, and D. J. Hawkes. Voxel-based 2-D/3-D registration of fluoroscopy images and CT scans for image-guided surgery. *IEEE Trans. Information Technology in Biomedicine*, 1(4):284–293, Dec. 1997.

[7] J. West, J. M. Fitzpatrick, M. Y. Wang, B. M. Dawant, C. R. Maurer, R. M. Kessler, and R. J. Maciunas. Retrospective intermodality registration techniques for images of the head: Surface-based versus volume-based. *IEEE Trans. Medical Imaging*, 18(2):144–150, Feb. 1999.

Proceedings of the 2005 11th International Conference on Parallel and Distributed Systems (ICPADS'05)
0-7695-2281-5/05 $20.00 © 2005 IEEE

07(IV)-19

直達式骨折整復の臨床データ取得システム

○ 鄭 常賢[a], 廖洪恩[b], 小林英津子[b], 光石衛[b], 中島義和[b], 小山毅[d], 菅野伸彦[d], 前田ゆき[e], 別所雅彦[c], 大橋暁[c], 松本卓也[c], 大西五三男[c], 佐久間一郎[b]

東京大学大学院{[a]新領域創成科学研究科, [b]工学系研究科, [c]医学系研究科}, [d]大阪大学大学院医学系研究科, [e]大阪南医療センター

A Clinical Data logging system of Direct fracture reduction.

S.Joung[a], H.Liao[b], E.Kobayashi[b], M.Mitsuishi[b], Y.Nakajima[b], T.Koyama[d], N.Sugano[d], Y.Maeda[e], M.Bessho[c], A.Ohashi[c], T.Matsumoto[c], I.Ohnishi[c], I.Sakuma[b]

{[a]Graduate School of Frontier Sciences, [b]Graduate School of Engineering, [c]Graduate School of Medicine}, the University of Tokyo,

[d]Graduate School of Medicine, Osaka University, [e]National Organization Osaka Minami Medical Center

Abstract: Clinical data quantification of a fracture reduction has become important as the development of new fracture reduction technology such as navigation and robot assisted fracture reduction. A reduction force and a reduction path are the key points in considering the control and safety of these new reduction methods. We have developed a clinical data logging system(CDLS) of direct fracture reduction, which reduces using ring-frame connected bone fragment directly. The CDLS synchronously records the reduction force, the reduction path and two video signals. One records the images from C-arm and the other records whole surgery process. This paper introduces the structure of CLDS and the resultants of application to fracture model.

Key words: Clinical data, Fracture reduction, Reduction force, Reduction path.

1. 序論

骨折治療は近年大きく発展してきており，低侵襲で整復の精度を上げることが可能となってきた．特に最近は，術中に骨片の位置が認知できるナビゲーションシステムを用いた治療方法に関する研究が盛んに行われている[1]．骨折治療法は様々であるが，どの治療法でも整復を伴い整復の結果が治療の成果に大きく影響する．大腿骨頚部骨折の整復に関しては大きい整復力が必要で術者への負担が過大になる．そこで，ロボットを用いた整復支援システムに関する研究が報告されている [2, 3]．このような整復支援ロボットには過渡の整復力を防ぐための安全装置が装着されている．一定以上の整復力が働いたときにその軸がフリー状態になるフェイルセイフ装置が一例である[3]．

ロボットの制御方法と安全装置の仕様を決めるためには，整復手術中の整復パス，整復力などの臨床データを参照するべきであり，今までは大きく必要とされていなかった骨折整復術中の臨床データを記録し定量化する必要性が整復技術の発展と共に高くなってきた．このため，Thomas らは整復力を定量化した[4]．しかし，整復パスを記録していないため骨片の位置と整復力との関係は解析されていない．そこで我々は骨片に打ったピンをリングフレームで固定し，そのフレームを持ち骨折整復を行う直達式整復術中の整復力とパスを記録するシステムを開発した[5]．しかし，整復力を計測するセンサの滅菌を検討してなかったので，臨床使用には適してなかった．本研究では，臨床使用可能とするように改良し，さらに画像入力も可能としたシステムを紹介し，模擬骨を用いた整復への応用結果を報告する．

2. 臨床データ取得システム

臨床データ取得システム(Clinical Data loggings system, CDLS)では骨折整復時に発生する整復力，整復パス，C-arm画像と現場の様子を記録することが望ましい．我々の開発した CDLS は，PC,画像入力ボード(PCI-5531, Interface)，整復力を測るための力覚センサ(IFS-67M25T50, Nitta, 定格 Fx, Fy [N]: 450; Fz [N]: 900; Mx - Mz [Nm]:40)，整復パスを追跡するための光学式 3 次元位置計測装置(Polaris, NDI, Canada)で構成され，以上のデータを計測可能とした．これらのデータは位置と整復力との関係などを分析するため，同期を取って記録する必要があり，システムではひとつのプロセスでコンピュータ側からデータ要求信号を送りそのときのデータを取得する方法を用いた．

Thomas らの研究結果によると骨片の牽引力の最大値は396N，回旋トルクの最大値は74Nmなので使用した力覚センサの定格は十分である．しかし，力センサの適切な滅菌法がないため，滅菌可能なカバーを製作した．カバーはアシスタントの補助により，術者の手を汚すことなく，取り付けられる．Fig. 1にカバーを取り付けた力覚センサと整復装置の外観を示す．図の右はカバーを外したときのセンサとカバーの様子である．カバーには整復パスを記録するため，光学式 3 次元位置計測装置のマーカを付着した．骨片の位置と整復力を計算するための概念図を

Fig. 2 に示す. 光学式 3 次元位置計測装置, 力覚センサ, C-armと骨片の座標系を各々ΣP, ΣS, ΣC, ΣBと設定する. ΣPからΣSとΣC への変換行列 ${}^{P}T_{S}$ と ${}^{P}T_{C}$ は 3 次元計測器から計測できる. ΣC からΣBへの変換行列 ${}^{C}T_{B}$ は2D/3Dレジストレーションなどの手法で求められる. 以上の変換行列で力覚センサの座標系から骨座標系への変換行列 ${}^{S}T_{B}$ が式(1)で計算できる.

$$ {}^{S}T_{B} = \left({}^{P}T_{S}\right)^{-1} {}^{P}T_{C}\, {}^{C}T_{B} \tag{1} $$

そこで骨片と整復装置を剛体として考えると, ${}^{S}T_{B}$ を一回計算しておくことにより, 整復中はセンサのマーカを追跡することたけで光学式 3 次元位置測装置から見た骨の位置と姿勢が式(2)で求められる.

$$ {}^{P}T_{B} = {}^{P}T_{S}\, {}^{S}T_{B} \tag{2} $$

整復力に関しても, 式(3)(4)により, センサから計測した力が骨座標系の力に変換できる.

$$ {}^{B}T_{S} = ({}^{S}T_{B})^{-1} = \begin{bmatrix} {}^{B}R_{S} & {}^{B}P_{S} \\ 0 & 1 \end{bmatrix} \tag{3} $$

$$ \begin{bmatrix} {}^{bone}\mathbf{f} \\ {}^{bone}\mathbf{n} \end{bmatrix} = \begin{bmatrix} {}^{B}R_{S} & \mathbf{0} \\ \left[{}^{B}P_{S}\times\right]{}^{B}R_{S} & {}^{B}R_{S} \end{bmatrix} \begin{bmatrix} {}^{sensor}\mathbf{f} \\ {}^{sensor}\mathbf{n} \end{bmatrix} \tag{4} $$

3. 骨折モデルの整復への応用

骨折モデルは X 線で確認できる材質のモデル骨を骨折させ, 筋肉代わりにゴムを貼り付けることで製作した. 大腿骨頚部骨折の場合, 骨片は中殿筋, 外閉鎖筋などの働きにより上半身のほうに引っ張られ, 外旋されるのでその働きをゴムで模擬した. 今回の実験では骨の座標はペンマーカを用いて指定した. 整復は整形外科医により行い, そのときのデータを CDLS により取得した. C-armは使わず, 代わりにカメラからの画像を入力した.

データの取得周期 0.3s で 2 枚の画像, 整復力と整復パスを記録することができた. Fig. 3 に取得した整復力を示す. 整復力はy軸の力(牽引方向)とモーメント(内旋方向)に大きく必要とすることが解る. 整復パスはマーカが術者に隠され一部記録できてない部分があった.

4. 考察と結論

実験では模擬骨を用いたので, 計測した整復力の大きさには意味がないが, どの成分の整復力が働くか確認することができた. また整復時の骨片の動きも確認することができた. センサのマーカは術者に邪魔にならない横方向に移すべきである. データ取得周期は 0.3 秒で遅いが, 整復の動作がゆっくり行われるので問題にはならない. 周期をあげるためには複数のパソコンにより並列処理をすればよいが, システムが大きくなるので手術現場では適さない.

今後は, C-armとレジストレーション方法を用いた模擬整復でシステムを評価し, 実際に臨床でデータ取得を行う予定である.

謝辞

本研究の一部は厚生労働科学研究費補助金(生体機能解析・補助・代替機器開発研究事業)(17100301)による.

文献

1) P.Grützner, et al.:"Computer aided long bone fracture treatment", Injry, Int.J.Care injured(2004) 35, S-A57-S-A64, 2004
2) B. Füchtmeier, et al.:"Reduction of femoral shaft fractures in vitro by a new developed reduction robot system 'RepoRobo'", Injury, Int.J.Care Injured (2004)35, S-A113-S-A119, 2004
3) Mamoru MITSUISHI, et al.: "Development of a Computer-Integrated Femoral Head Fracture Reduction System", Proceedings of the 2005 IEEE International Conference on Mechatronics,834-839, 2005
4) Thomas Gösing, et al.: "Force and Torque during Fracture Reduction: Intraoperative Measurements in the Femur", Journal of Orthopaedic Research, 333-338,2006
5) 森本顕二郎 他, " 直達式骨折整復支援装置に関する研究" 第15回日本コンピュータ外科学会大会論文集, 2006

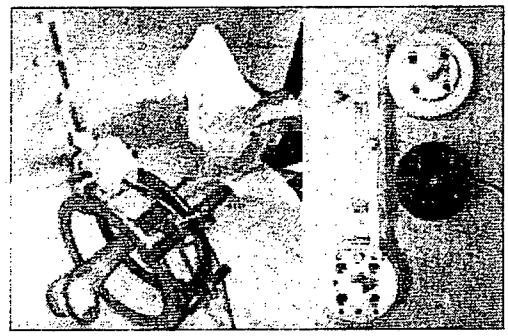

Fig. 1 Fracture reduction device.

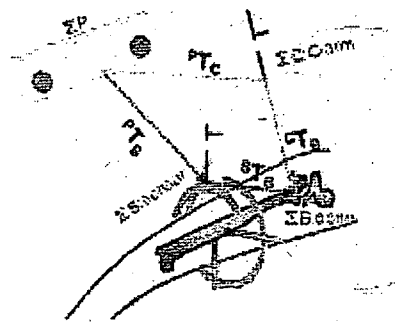

Fig. 2 Coordinate and translation matrix.

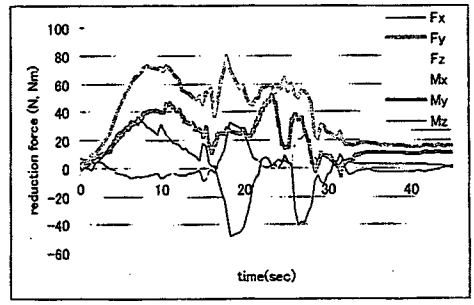

Fig.3 The reduction force during fracture reduction

直達式骨折整復を支援する骨折整復システムの開発

鄭 常賢[1]、加門 大和[1]、廖 洪恩[2]、光石 衛[2]、中島 義和[2]、
小山 毅[4]、菅野 伸彦[4]、前田 ゆき[5]、別所 雅彦[3]、大橋 暁[3]、松本 卓也[3]、
岩城 純一郎[6]、中沢 東治[6]、大西 五三男[3]、中村 耕三[3]、佐久間 一郎[2]
東京大学大学院 {[1] 新領域創成科学研究科、[2] 工学系研究科、[3] 医学系研究科}
[4] 大阪大学大学院 医学系研究科、[5] 大阪南医療センター、[6] THK(株)

骨粗鬆症がある患者におこりやすい骨折のなかでも大腿骨頚部骨折は寝たきりとなる可能性の高い骨折である。社会の高齢化の進行に伴い骨粗鬆症の患者が増加すると、大腿骨頚部骨折の患者も増加すると予測されている。

大腿骨頚部骨折の治療法は外科的な手術によるものがほとんどである。手術では大腿骨の遠位骨片を牽引しながら位置決めし、ピンによって固定する。しかし、大腿筋などの周辺組織が萎縮した状態では整復のための牽引に大きな力が必要となるため術者にとって負担となる。また、X線透視下で2次元の情報を用いて位置決めを行わなければならないため、術者の熟練が必要であり、手術を行うことで術者が受けるX線被爆も問題である。

これらの問題に対し、我々は骨折整復システムの開発を行った(Fig. 1)。システムは骨折整復ロボットとナビゲーションシステムに構成されている。骨折整復には、足首をつかみ遠位骨片の位置を合わせる介達式骨折整復方法と、骨片にピンを打ち、ピンに連結されたリングを持って直接整復を行う直達式骨折整復方法がある。骨折整復システムは介達式骨折整復に対して使えるように構成されているが、ロボットを使う利点を考えると骨片の正確な位置決めが可能な直達式骨折整復にも使用されるように構成する必要があり、今回は新たに直達式骨折整復を直達式骨折整復ロボットに実装を行った。

骨折整復ロボットは並進3自由度と回転3自由度の6自由度を有する。骨片の牽引と回旋をするときの整復力が設定値より大きくなると各関連軸をフリーにするフェイルセイフ装置が装着されており安全性を保つ。動作モードはタッチパネルを用いたジョグモード、術者の整復力をパワーアシストする手動モード、ナビゲーションからの指令により自動で整復を行う自動整復モードがある。

直達式整復では、骨とロボットの手先は専用のジグで繋がっているので、骨の長軸とロボットの牽引軸が一致しない。骨片の姿勢だけを変えるため、骨折断面の中心を仮想中心と見なし、ロボットを制御する拘束パワーアシストを実装し、有効性を検証した。

ナビゲーションシステムは術前にCTからの3次元モデルを用いて整復ゴールを計算する。術中にはC-armで撮った画像と3次元モデルをレジストレーションすることにより、実空間での骨片間の位置関係を認知する。骨片の現在位置からゴールまでの整復パスは術者の意見を反映して作成され、整復ロボットに指令を送り整復を行う。構成したシステムは骨折モデルでの整復実験でその有効性を示す。

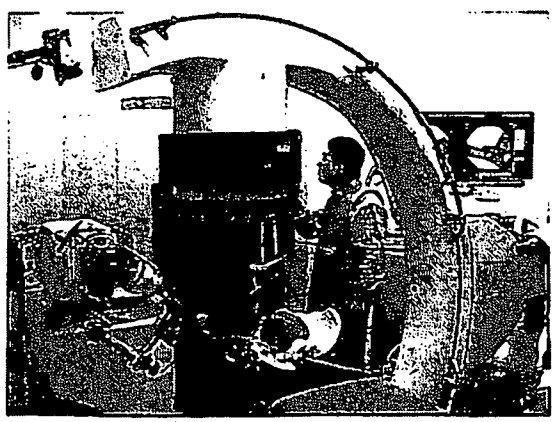

Fig.1. 骨折整復システム

Communications

Fluoroscopic Bone Fragment Tracking for Surgical Navigation in Femur Fracture Reduction by Incorporating Optical Tracking of Hip Joint Rotation Center

Yoshikazu Nakajima*, Takahito Tashiro, Nobuhiko Sugano, Kazuo Yonenobu, Tsuyoshi Koyama, Yuki Maeda, Yuichi Tamura, Masanobu Saito, Shin'ichi Tamura, Mamoru Mitsuishi, Naohiko Sugita, Ichiro Sakuma, Takahiro Ochi, and Yoichiro Matsumoto

***Abstract*—A new method for fluoroscopic tracking of a proximal bone fragment in femoral fracture reduction is presented. The proposed method combines 2-D and 3-D image registration from single-view fluoroscopy with tracking of the head center position of the proximal femoral fragment to improve the accuracy of fluoroscopic registration without the need for repeated manual adjustment of the C-arm as required in stereo-view registrations. Kinematic knowledge of the hip joint, which has a positional correspondence with the femoral head center and the pelvis acetabular center, allows the position of the femoral fragment to be determined from pelvis tracking. The stability of the proposed method with respect to fluoroscopic image noise and the desired continuity of the fracture reduction operation is demonstrated, and the accuracy of tracking is shown to be superior to that achievable by single-view image registration, particularly in depth translation.**

***Index Terms*—Fluoroscopic bone fragment tracking, fracture reduction, kinematic knowledge of the hip joint, motion constraint.**

I. Introduction

Computer guidance for femur fracture reduction has been studied as a means of improving repositioning accuracy and reducing radiation exposure to medical staff by shortening procedures and introducing robotic surgery. Where previous studies have focused on femoral shaft fractures, proximal femur fractures such as femoral intertrochanteric fractures are also common, particularly in osteoporotic elder females. In previously proposed systems, reference markers for the positional sensor are attached to both proximal and distal bone fragments to measure the spatial relationship between the fractured bone fragments. In a proximal femur fracture, however, it is difficult to attach the reference marker to the proximal fragment, as the fragment is located deep in the body and the implantation required for attachment may have an undesirable effect on the hip joint in leg position changes during surgery.

Some researchers have investigated a fluoroscopic tracking method for bones [1], [2]. The methods involve the use of 2-D/3-D registration, which in conventional single-view procedures does not provide sufficient accuracy in depth translation for clinical use of the fracture fragment tracking. Although stereo-view 2-D/3-D registration overcomes some of the shortcomings of single-view registration, interactive C-arm positioning is required in each registration step. The method proposed by the present authors effectively combines 2-D/3-D registration from a single-view fluoroscopic image with the proximal femoral fragment position obtained by pelvis tracking. The use of such a 2-D/3-D registration technique by incorporating positional information at a number of points was originally proposed by Russakoff [3] as a means to improve the accuracy of stereo-view registration. However, in that pioneering study, fiducial markers were embedded directly in the bone to acquire the positional information. In contrast, our method employs pelvis position tracking as a less-invasive approach, and knowledge of the kinematics of the hip joint is applied to acquire the position of the femoral head center. The proposed method therefore does not require the implantation of a fiducial marker in bones such as the proximal femur fragment.

Manuscript received November 24, 2005; revised November 15, 2006. This work was supported in part by the Japan Society for the Promotion of Science (JSPS) under the Research for the Future Program JSPS-RFTF99I00903 and in part by the JSPS Grants-in-Aid for Scientific Research and the Encouragement of Young scientists (A) 17680009 and (B) 14780281. *Asterisk indicates corresponding author.*

*Y. Nakajima is with the School of Engineering and the Intelligent Modeling Laboratory, The University of Tokyo, Tokyo 113-8657, Japan (e-mail: nakajima@iml.u-tokyo.ac.jp).

T. Tashiro is with the Applied Information System Division, Cybermedia Center, Osaka University, Osaka 565-0871, Japan.

N. Sugano and T. Koyama are with the Graduate School of Medicine, Osaka University, Osaka 565-0871, Japan.

S. Tamura is with the Graduate School of Medicine and the Department of Medical Engineering, Osaka University, Osaka 565-0871, Japan.

K. Yonenobu, Y. Maeda, M. Saito and Y. Tamura are with the Osaka Minami Medical Center, Osaka 586-8521, Japan.

M. Mitsuishi, N. Sugita, and I. Sakuma are with the School of Engineering, the University of Tokyo, Tokyo 113-8656, Japan.

T. Ochi is with the Sagamihara National Hospital, Kanagawa 228-8522, Japan.

Y. Matsumoto is with the School of Engineering and the Intelligent Modeling Laboratory, the University of Tokyo, Tokyo 113-8656, Japan.

Digital Object Identifier 10.1109/TBME.2007.900822

II. Method

A. Process Overview

The segmentation of the pelvis and fragments of the fractured femur are processed preoperatively using a computed tomography (CT) volume and in-house segmentation software. The femoral head center, employed as the hip joint rotation center, is localized by sphere-fitting image processing in the CT volume coordinate system. Bone tracking during surgery is performed in two registration steps. In the first registration step, two imaging operations and a position measurement procedure are performed once for conventional stereo-view 2-D/3-D registration to determine the initial pose of the segmented bone volume and the geometric relationship between the pelvis reference marker and the hip rotation center point. Single-view fluoroscopy imaging and a single position-tracking procedure are then performed for each iteration of the hybrid bone tracking described below. This procedure is performed iteratively for bone tracking during surgery.

B. Hybrid Bone Tracking Method

The method employs two constraints: an image similarity measure, and a positional constraint for the hip joint rotation center based on optical tracking. Gradient correlation is employed as an image similarity measure, and is sensitive to thin-line intensity differences such as bone edges, although it is potentially insensitive to the overlap of soft tissue.

Let E_{image} represent the evaluation value for image similarity measure. The positional constraint of the hip joint rotation center can then be expressed as

$$E_{\text{position}} = \text{dist}(p'_{i,c}, p_{i,c}). \quad (1)$$

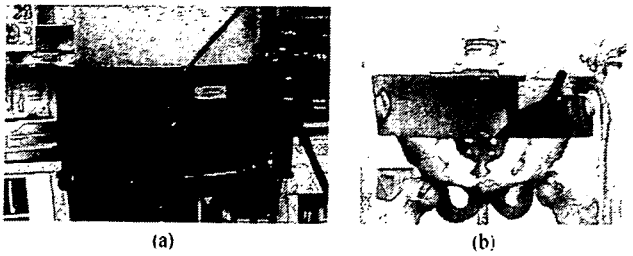

(a) (b)

Fig. 1. Reference markers on the (a) fluoroscope and (b) pelvis.

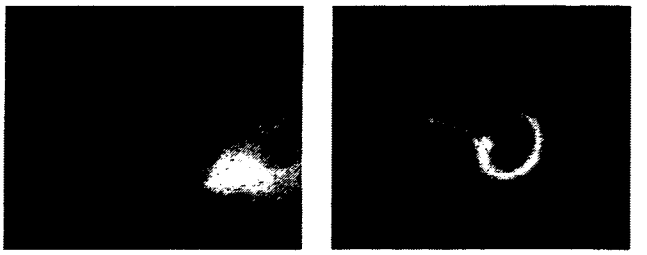

(a) (b)

Fig. 2. DRRs for simulation. (a) Original volume. (b) Segmented volume (proximal fragment only).

where $\mathrm{dist}(\cdot)$ is the Euclidean distance between two points, and p'_{rc} and p_{rc} are the hip rotation center assumed in computation and the position tracked by the optical localizer. Let $T_{\mathrm{pelvis\_tracker}}$ be the latest transformation matrix of the pelvis reference marker. The tracked position can then be obtained by

$$p_{rc} = T_{\mathrm{pelvis\_tracker}}\, {}^{\mathrm{pelvis\_tracker}}p_{rc} \tag{2}$$

where ${}^{\mathrm{pelvis\_tracker}}p_{rc}$ is determined by the femoral head center localization in the CT volume and the first registration step.

A hybrid similarity measure that combines the constraints given by the hip joint rotation center tracking and the 2-D/3-D registration can then be defined as

$$E_{\mathrm{hybrid}} = -E_{\mathrm{image}} + \gamma E_{\mathrm{position}} \tag{3}$$

where γ is a weighting coefficient.

The optimizing computation is based on the Powell method [4]. A weighted search method [2] is employed for coarse optimization, and a polynomial function fitting method [5] is then adopted for improvement of depth accuracy.

III. Experiments

A. Image and Position Data Acquisition

CT volumes were acquired using a HiSpeed Plus scanner (General Electric Co., USA) with a voxel size of $0.68 \times 0.68 \times 1\ \mathrm{mm}^3$ for the fractured part and the femoral head, and $0.68 \times 0.68 \times 3\ \mathrm{mm}^3$ for other parts. Fluoroscopic images were taken intraoperatively using a Siremobil Iso-C instrument (Siemens AG, Germany). The image size was 640×512 pixels. The positions of the fluoroscope and the pelvis were obtained for each registration step using an optical localizer (Optotrak, Northern Digital Inc., Waterloo, ON, Canada). The reference markers (Fig. 1) were attached to the image intensifier cylinder of the fluoroscope and the pelvis (C-arm Tracker and VersaTrax Tracker, Traxtal Technologies Inc., Toronto, ON, Canada). The pelvis tracker shown in Fig. 1(b) can be fixed to the patient's lumbus using a silicone belt with Velcro tape for hipline length adjustment. The silicone belt has two fixation holes that fit to the anterior-superior-iliac spine around the left and right sides of the pelvis to ensure that the tracker is immobilized against the patient's body.

B. Simulations

CT images of five patients and two phantoms were used in simulations of the proposed tracking method. For use as fluoroscopic images to be input into the simulation, digitally reconstructed radiographs (DRRs) of each original CT volume were generated from arbitrary viewpoints determined so as to emulate the real dimensions of fluoroscopy during surgery. The initial positions of the fragment registration were determined by random perturbation from the original position in the CT volume. The standard deviation of the perturbation was 3 mm for translation and 3° for rotation. The overlap of bone or soft tissue in fluoroscopy hampers 2-D/3-D registration. For estimating such influences, segmented CT volumes of the fragments of the fractured femur, pelvis, and soft tissue were used in simulated fluoroscopy. The DRRs were then generated from the CT volumes of the proximal fragment and the entire abdominal structure. In DRR generation, the CT volumes of the proximal fragment were used to estimate the accuracy of principal registration, and the original CT volumes were used to estimate the overall accuracy and the influence of soft tissue overlap. Examples of DRRs are shown in Fig. 2. The error at the femoral head center was computed statistically by comparing estimated positions with the original position. For accuracy validation, 100 trials of registration were performed for each parameter set.

The results are summarized in Tables I and II. Averages, standard deviations and, worst error are shown. The estimation accuracy was affected by the overlap of soft tissue and bone. Nevertheless, the proposed method was more robust than the single-view method, and provided results closer to the real position. The component error of depth translation in the fluoroscopy coordinate system in particular was substantially improved, for example, from 1.49 mm to 0.007 mm in the case of the full abdominal patient CT. The accuracy was also found to depend on the spatial distribution of X-ray absorption in the target object. In the case of the proximal fragment bone, the distribution may have rotational symmetry around the femoral neck axis, and the maximum principal component of error variance was oriented parallel with this axis. In the phantom CT experiment, the maximum principal components of the error distribution were 2.73° and 0.80° in the single-view and proposed methods, respectively, representing contributions of 82.02% and 79.03%. After removing the maximum principal component, the residual errors were 1.28° and 0.41°, respectively. In the patient CT experiment, the maximum principal components of the error distribution were 1.06° and 0.71°, corresponding to contributions of 44.68% and 40.22%, and the residual errors were 1.18° and 0.86°, respectively.

C. In-Vitro Experiment

Two phantoms were used to simulate scenes of proximal femur fracture in an *in vitro* experiment. Plastic pelvis and femur models (Sawbones Pacific Research Laboratories, Vashon, WA) were fractured and aligned using Styrofoam plates. The alignment of the fractured fragments was determined based on a typical intertrochanteric fracture. To find the "gold standard" registration, four fiducial markers (30-mm glass balls) were embedded in the Styrofoam cover of the phantom, ensuring that the markers did not overlap in the pelvis and femur silhouettes in fluoroscopy. Four light-emitting diode markers were also attached to the front of the phantom Styrofoam cover as reference markers for optical tracking.

Fig. 3 shows the experiment setup, where arrows indicate the positions of reference markers. The phantom was placed on a carbon bed (Mizuho, Japan), and the positions of the fluoroscope and phantom

[7] S. Warisawa, T. Ishizuka, M. Mitsuishi, N. Sugano, K. Yonenobu, and T. Nakazawa, "Development of a femur fracture reduction robot," in *Proc. IEEE Int. Conf. Robotics and Automation (ICRA 2004)*, 2004, pp. 3999–4004.

[8] F. Ino, Y. Kawasaki, T. Tashiro, Y. Nakajima, Y. Sato, S. Tamura, and K. Hagihara, "A parallel implementation of 2-D/3-D image registration for computer-assisted surgery," *Int. J. Bioinformatics Res. Appl.*, vol. 2, no. 4, pp. 341–358, 2006.

Redefining Performance Evaluation Tools for Real-Time QRS Complex Classification Systems

Philippe Ravier*, Frédéric Leclerc, Cedric Dumez-Viou, and Guy Lamarque

***Abstract*—In a heartbeat classification procedure, the detection of QRS complex waveforms is necessary. In many studies, this heartbeat extraction function is not considered: the inputs of the classifier are assumed to be correctly identified. This communication aims to redefine classical performance evaluation tools in entire QRS complex classification systems and to evaluate the effects induced by QRS detection errors on the performance of heartbeat classification processing (normal versus abnormal). Performance statistics are given and discussed considering the MIT/BIH database records that are replayed on a real-time classification system composed of the classical detector proposed by Hamilton and Tompkins, followed by a neural-network classifier. This study shows that a classification accuracy of 96.72% falls to 94.90% when a drop of 1.78% error rate is introduced in the detector quality. This corresponds to an increase of about 50% bad classifications.**

***Index Terms*—Classification, hardware implementation, heartbeat recognition, neural network, QRS complex detection.**

I. Introduction

The problem of heartbeat classification has been widely explored in the literature [1]–[8]. However, real-time classification systems often necessitate the detection of the cardiac beats before any classification procedure. The cardiac beats are also refered to QRS complex shapes where the letters stand for the three successive main phases of a cardiac cycle. In such classification systems, classical performance evaluation tools become irrelevant since the detection errors are not taken into account in the classification statistics. In this communication, we therefore propose to:

- redefine the classical performance evaluation tools taking the entire classification system into consideration;
- experimentally discuss the influence of the detection stage on classification results;
- give material for finding the best compromise between the quality of the detector, the quality of the classifier, and the computational time in real-time classification systems.

In order to achieve these goals, we implemented a simple real-time classification system on an electronic board. The proposed system is composed of a QRS complex extractor (detection part) followed by a normal or abnormal peak recognition step (classification part). Abnormal beats are opposed to normal beats according to their QRS waveform shapes.

For instance, a normal/abnormal classification system may be useful for Holter monitoring where only the critical parts as well as the cardiac history (i.e., peak-to-peak intervals) are of medical interest. It is not worth recording the healthy electrocardiographic (ECG) samples. The amount of data can therefore be drastically reduced and the entire breakdown will be shorter since the physician will devote his or her expertise to the critical parts of the ECG signal, while also taking into account the peak-to-peak intervals of the entire monitoring.

Several algorithms have been proposed in the literature for the detection and classification of ECG beats. Since our system has to be embedded with real-time processing constraints, the computation cost must be low. Various approaches (wavelets [9], [10]; filter banks [11]; and neural networks [12]) have been investigated to improve the quality of the detectors. However, the gain obtained is generally offset by the greater complexity of the algorithms, involving higher computational costs. It is the reason why the well-known Hamilton and Tompkins [13], [14] detector has been chosen here. Similarly, many methods have been investigated for the classification part (neural networks [1]–[3], fuzzy theory [3], [5], support vector machine [4], higher order spectral techniques [6], and hidden Markov models [7], ...). A neural-network approach has been adopted in this study because its parallel processing implementation is well adapted to real-time constraints. Finally, we tested the system on the Massachusetts Institute of Technology–Beth Israel Hospital Arrythmia Database (MIT–BIH) [15] since this database is commonly used for performance evaluations of detection or classification algorithms.

This communication is organized as follows. The classification system is introduced in the second part. Such a system leads to the redefinition of the performance evaluation tools in the third part. These new tools are tested on real data in the fourth part, considering real-time classification of the MIT/BIH recordings. The communication ends with discussions and conclusions.

II. Normal/Abnormal Real-Time Beat Classification System

After digitizing the analog ECG signal through a 16–b analog-to-digital converter (ADC) using a 360-Hz sampling rate, the algorithmic part is divided into two main functions (Fig. 1).

1) The ECG beat extractor detects QRS complex waveforms and extracts ECG waveform patterns after they have been normalized and centered about the fiducial point. Two versions of the Hamilton and Tompkins detector have been real time implemented [13], [14]: the first one includes the search back procedure (SB+) and the second one does not (SB−).
2) the neural-network classifier that is fed by Fourier coefficients of the ECG waveform patterns provided by the previous stage. The classifier is a multilayer perceptron (MLP) [16] with 16 input nodes (16 first absolute values of the 128 Fourier samples excluding the dc component), four neurons in the hidden layer, and one output neuron. Each neuron labeled 1 to 5 has four inputs and one output with the classical associated sigmoidal activation function $y_j(n) = (1)/(1 + e^{-v_j(n)+\theta_j})$, where n is the number of QRS pattern to be classified and j is the neuron number. The value $v_j(n)$ is the net internal activity level of neuron j and is equal to $v_j(n) = \sum_{i=1}^{4} w_{ji} x_{ji}(n)$, for $j = 1$ to 4 and $v_5(n) =$

Manuscript received May 12, 2006; revised December 18, 2006. *Asterisk indicates corresponding author.*

P. Ravier is with the Laboratory of Electronics, Signals and Images, University of Orleans, Orléans Cedex 45067, France (e-mail: philippe.ravier@univ-orleans.fr).

C. Dumez-Viou and G. Lamarque are with the Laboratory of Electronics, Signals and Images, University of Orleans, Orléans Cedex 45067, France (e-mail: cedric.dumez-viou@obs-nancay.fr; guy.lamarque@univ-orleans.fr).

F. Leclerc is with the Laboratory of Electronics, Signals and Images, University of Orleans, Orléans Cedex 45067, France and also with the Department of Aerospace Physiology, Institute of Aerospace Medicine of the Army Health Department, Brétigny-Sur-Orge Cedex 91223, France (e-mail: frederic.leclerc@univ-orleans.fr).

Digital Object Identifier 10.1109/TBME.2007.902594

TABLE I
ESTIMATION ERROR FOR TRANSLATION IN SIMULATION

	Phantom [mm] (proximal fragment only)	Phantom [mm]	Patient [mm] (proximal fragment only)	Patient [mm]
Single-view method	0.12±0.32 (1.03)	1.07±2.76 (11.314)	0.0061±0.27 (0.74)	1.91±2.43 (8.29)
Proposed method	0.00047±0.013 (0.11)	0.044±0.058 (0.21)	0.00046±0.0061 (0.029)	0.51±0.30 (0.86)

TABLE II
ESTIMATION ERROR FOR ORIENTATION IN SIMULATION

	Phantom [degrees] (proximal fragment only)	Phantom [degrees]	Patient [degrees] (proximal fragment only)	Patient [degrees]
Single-view method	0.18±1.11 (3.243)	1.40±3.02 (10.2)	0.0068±0.15 (0.41)	1.80±1.59 (5.37)
Proposed method	0.10±0.96 (2.92)	2.55±0.90 (5.06)	0.075±0.98 (1.90)	1.47±1.11 (3.45)

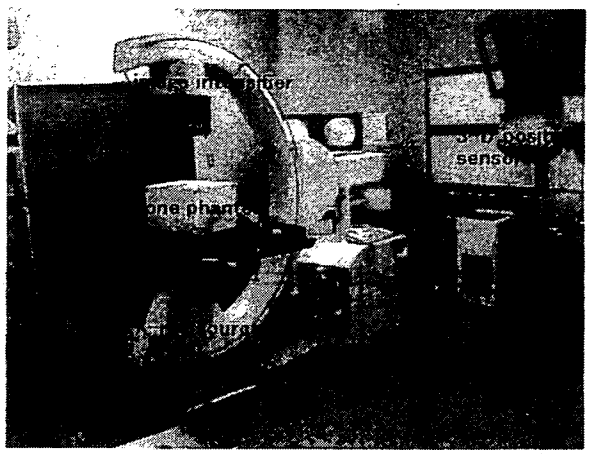

Fig. 3. *In vitro* experiment setup.

TABLE III
ESTIMATION ERROR IN IN VITRO PHANTOM TEST

	Translation error [mm]	Orientation error [degrees]
Single-view method	2.52±2.02 (10.41)	2.54±1.92 (6.32)
Proposed method	1.83±0.51 (3.37)	1.29±1.70 (4.23)

were localized using an optical sensor. The phantom reference marker was used as the reference marker for the pelvis, and also to track the rotation center of the hip joint. Fluoroscopy was performed simultaneously.

The errors are summarized in Table III. The translation error was successfully improved by applying the proposed method. The maximum principal components of error variance for rotation were 1.58° and 1.45° for the single-view and proposed methods, representing contributions of 50.97% and 72.35%, respectively. The remaining error was 1.55° and 0.89°, respectively.

IV. DISCUSSION

Although some of the worst case results appear to have converged at local minima and are not clinically acceptable, most of the results converged to acceptable values. In our experiments, the convergence behavior from initial bone positions was predictable in most cases, and manual adjustment of the initial position corrected the result.

The bias error in the *in vitro* phantom test was greater than that indicated by the simulations. This can be primarily attributed to positional error in optical tracking, and is also a result of the use of DRRs as input images in the simulation, whereas real fluoroscopic images were used in the *in vitro* test.

The overlap of soft tissue and other bones resulted in the appearance of untrue edges in the CT volumes. In the single-view method, convergence to local minima is caused in part by the overlap of other anatomical structures, particularly the edge of the pelvis acetabular. The proposed method avoids this effect and achieves successful registration in such situations, primarily as a result of the positional constraint imparted by hip rotational center tracking.

As the constraint E_{position} effectively compensates for the positional inaccuracy in E_{image}, 2-D/3-D registration accuracy is improved by the proposed method, particularly with respect to depth. This approach does not require interactive C-arm re-positioning, and therefore will be advantageous for reducing the time required for fracture reduction by robotic surgery [7].

For real-time bone tracking, registration should be performed at least 30 times/second. The computation time for the proposed method at present is 300 s/registration by a PC (Xeon 3.2 MHz CPU, 2 GB memory), and less than 10 s when computed on a parallel platform consisting of 128 CPUs [8]. Therefore, some supplemental technologies are required in order to introduce robotic surgery into practical clinical settings. The robotic manipulators should move slowly for safety, and some form of prediction (or extrapolation) techniques should be introduced for bone motion to reduce imaging frequency. As the method requires frequent imaging, the X-ray exposure dose to both the patient and surgeons must also be considered. The Siremobil Iso-C instrument employed for pulse-mode fluoroscopy emits a strong but instantaneous X-ray pulse that affords good-quality images at a reduced total X-ray dose compared to continuous fluoroscopy. The X-ray dose for the present procedure is 0.92 mGy/min with imaging at 1 Hz, less than a half that of regular fluoroscopy (2.38 mGy/min).

REFERENCES

[1] S. Lavallée and R. Szeliski, "Recovering the position and orientation of free-form objects from image contours using 3D distance map," *IEEE Trans. Pattern Anal. Mach. Intell.*, vol. 17, no. 4, pp. 378–390, Apr. 1995.

[2] J. Weese, G. P. Penney, P. Desmedt, T. M. Buzug, D. L. G. Hill, and D. J. Hawkes, "Voxel-based 2-D/3-D registration of fluoroscopy images and CT scans for image-guided surgery," *IEEE Trans. Inf. Technol. Biomed.*, vol. 1, no. 4, pp. 284–293, Dec. 1997.

[3] D. B. Russakoff, T. Rohlfing, R. Shahidi, D. H. Kim, J. R. Adler Jr., and C. R. Maurer Jr., "Intensity-based 2D-3D spine image registration incorporating one fiducial marker," in *Proc. Medical Image Computing and Computer-Assisted Intervention (MICCAI) 2003*, vol. 2878, Springer LNCS, pp. 287–294.

[4] M. J. D. Powell, "An efficient method for finding the minimum of a function of several variables without calculating derivatives," *Comput. J.*, vol. 7, pp. 155–162, 1964.

[5] T. Yamazaki, T. Watanabe, Y. Nakajima, K. Sugamoto, T. Tomita, H. Yoshikawa, and S. Tamura, "Improvement of depth position in 2-D/3-D registration of knee implants using single-plane fluoroscopy," *IEEE Trans. Med. Imag.*, vol. 23, no. 5, pp. 602–612, May 2004.

[6] J. M. Fitzpatrick, J. B. West, and C. R. Maurer Jr., "Predicting error in rigid-body point-based registration," *IEEE Trans. Med. Imag.*, vol. 17, no. 5, pp. 694–702, Oct. 1998.